PCCP

ROYAL SOCIETY OF CHEMISTRY

PAPER

View Article Online
View Journal | View Issue

Cite this: *Phys. Chem. Chem. Phys.*, 2025, **27**, 25352

Effect of alkali metal poisoning on Cu-SSZ-13 in selective catalytic reduction with ammonia (NH_3-SCR)

Boji Wang,[a] Yao Zhang,[ab] Sarayute Chansai,[a] Junling Zhan,[c] Huaizhong Xiang,[ad] Tengfei He,[c] Yilai Jiao,[e] Yu Zhang*[c] and Xiaolei Fan*[af]

Received 4th September 2025,
Accepted 30th October 2025

DOI: 10.1039/d5cp03404c

rsc.li/pccp

Cu-SSZ-13 is widely recognized as an efficient catalyst for the selective catalytic reduction of NO_x with ammonia (NH_3-SCR). However, in practical stationary applications, it is frequently exposed to alkali metal contaminants, which can significantly influence its catalytic performance. In this study, the effects of different alkali metal salts ($NaNO_3$, KNO_3, NaCl and KCl) on Cu-SSZ-13 were systemically investigated (regarding the variation in the physicochemical properties and NH_3-SCR activity). A slight promotional effect (about 10% increase in NO_x conversion) was observed at low temperatures (<250 °C) for alkali metal poisoned samples, which is attributed to the enhanced presence of active $ZCu^{II}OH$ species, as evidenced by H_2-TPR analysis. Conversely, a marked deactivation (up to 50% decline in NO_x conversion) was observed at high temperatures (>400 °C), primarily due to the loss of Brønsted acid sites and isolated Cu^{2+} species, as indicated by NH_3-TPD, pyridine-IR, H_2-TPR and UV-vis spectroscopy. Notably, alkali metal chlorides (KCl and NaCl) induced more severe deactivation than their nitrate counterparts, likely due to a synergistic effect between framework dealumination and transformation of Cu^{2+} species, leading to the formation of $CuAlO_x$ species. These findings provide deeper insight into the effect of alkali metal poisoning on the NH_3-SCR activity of Cu-SSZ-13, highlighting the necessity of preventing alkali metal chlorides from entering SCR systems to maintain catalyst efficiency.

1. Introduction

With the upcoming stringent environmental policies concerning NO_x emissions from both road transportation and industrial activities (like Euro 7/VII and EPA Tier 5 standards), the reduction of NO_x emissions is receiving heightened attention. Selective catalytic reduction using ammonia (NH_3-SCR) remains a common and effective technique with high NO_x conversions (up to 90%).[1,2] Conventional commercial V-based catalysts suffer from limitations such as poor hydrothermal stability and possible release of toxic vanadia species, hindering their applications in meeting the increasingly strict emission regulations globally.[3]

Transition metal (*e.g.*, Cu and Fe) promoted small-pore zeolites, particularly Cu-SSZ-13 (pore diameter = ~0.38 nm), are the state-of-the-art NH_3-SCR catalysts with characteristics like broad operational temperature windows, excellent hydrothermal stability and nontoxicity, and are promising alternatives to V-based SCR catalysts.[4–6] To ensure their practical deployment in industrial applications, it is imperative to investigate their resistance to various poisons. Alkali metals are among the most detrimental contaminants for NH_3-SCR catalysts, originating from both mobile sources (*e.g.*, urea solutions and biodiesel fuels) and stationary sources (coal-fired power plants, municipal waste incineration, and biomass combustion).[7–9]

Regarding deactivation mechanisms of Cu-SSZ-13 by alkali metals, current research findings suggest that they involve (i) the transformation of active Cu^{2+} ions to Cu oxides, and (ii) the pore blockage caused by Cu oxides and/or alkali metal oxides. Liu *et al.* investigated the poisoning effect of different potassium salts (K_2CO_3, K_2SO_4 and K_3PO_4) on Cu-SSZ-13 zeolites, and spectroscopic analyses (electron paramagnetic resonance, EPR and UV-visible diffuse reflectance spectroscopy, UV-vis)

[a] *Department of Chemical Engineering, School of Engineering, The University of Manchester, Oxford Road, Manchester M13 9PL, UK. E-mail: xiaolei.fan@manchester.ac.uk*
[b] *School of Civil Engineering, Weifang University of Science and Technology, Weifang 262700, China*
[c] *School of Chemistry and Pharmaceutical Engineering, Jilin University of Chemical Technology, Jilin 132022, China*
[d] *Department of Chemistry, Queen Mary University of London, London E1 4NS, UK*
[e] *Shenyang National Laboratory for Materials Science, Institute of Metal Research, Chinese Academy of Sciences, 72 Wenhua Road, Shenyang 110016, China*
[f] *Nottingham Ningbo China Beacons of Excellence Research and Innovation Institute, University of Nottingham Ningbo China, 211 Xingguang Road, Ningbo 315103, China*

showed the transformation of isolated Cu^{2+} into copper oxides, copper sulphates and copper phosphates in the salt-impregnated zeolites, underscoring the critical role of loss of isolated Cu^{2+} in catalytic deactivation.[3] Similar results were also reported by Wang *et al.*, who found that increased alkali loading promoted Cu^{2+} ion aggregation and subsequent decline in catalytic activity.[2] Similarly, Zhao *et al.* demonstrated that Na^+ ions enhanced Cu^{2+} reducibility and facilitated the formation of aggregated CuO_x species, which are prone to react with extra-framework aluminum (EFAL) to form $CuAlO_x$, as evidenced by UV-vis-NIR spectroscopy.[10] Based on H_2 temperature programmed reduction (H_2-TPR) analysis, Xie *et al.* observed that Na doping led to a marked reduction in the high-temperature reduction peak (~910 °C) associated with highly stable Cu species, suggesting their transformation into less active dispersed CuO or aggregated forms.[11] Additionally, Fan *et al.* found that, after impregnation of Na and K salts (1.50 mmol g_{catal}^{-1}), the specific surface area of the SSZ-13 zeolites decreased by 50% and 30%, respectively, indicating partially blocked micropores being responsible for deactivation.[12]

However, in current studies on alkali metal poisoning of SSZ-13 zeolites, alkali metal oxides, alkali metal sulphates and alkali metal phosphates are mainly employed, and alkali metal chlorides (*e.g.*, NaCl and KCl) are largely overlooked. NaCl and KCl can be released as volatile components during the combustion of coals[13,14] and the incineration of municipal solid wastes.[15] Also, previous research has shown that alkali chlorides might exhibit stronger poisoning effects than their oxide counterparts on vanadium-based SCR catalysts.[16,17] Hence, a systematic assessment of the effect of alkali chlorides on deactivating Cu-SSZ-13 is needed, especially for its NH_3-SCR applications to stationary sources.

This study investigates the effect of alkali metals, particularly alkali metal chlorides, on the SCR performance of Cu-SSZ-13, which could be potentially used as the SCR catalyst for emissions from stationary sources that are subject to harsh exhaust gas temperatures and complex compositions. To elucidate the deactivation mechanisms, comprehensive characterization studies were performed before and after alkali metal poisoning to assess the changes in physicochemical properties, such as powder X-ray diffraction (XRD), nitrogen (N_2) adsorption–desorption analysis, NH_3 temperature programmed desorption (NH_3-TPD), pyridine infrared spectroscopy (Py-IR), UV-vis, X-ray photoelectron spectroscopy (XPS) and H_2-TPR. The results suggest that (i) an increase in Z_2CuOH species might be responsible for the slight increase in the low-temperature activity of alkali metal poisoned samples, (ii) the deterioration of total acidity, particularly Brønsted acidity, and the depletion of isolated Cu^{2+} species are primarily responsible for the reduced high-temperature activity, and (iii) the synergetic interaction of framework dealumination and transformation of isolated Cu^{2+} species likely underlies the pronounced deactivation observed in Cu-SSZ-13 zeolites poisoned by alkali metal chlorides.

2. Experimental section

2.1 Preparation of materials

All reagents were purchased from Sigma-Aldrich and used without further purification unless otherwise specified. SSZ-13 zeolite was synthesized using a hydrothermal method described elsewhere.[18] In a typical synthesis, 0.6 g of NaOH and 9 g of TMAdaOH (25 wt% aqueous solution, Sachem Chemistry) were dissolved in 21.45 g of deionized (DI) water. Then, 0.3 g $Al(OH)_3$ (76.5 wt%) was gradually introduced into the solution under continuous stirring. Once fully mixed, 5.475 g silica sol (Ludox HS-40) was added under continuous stirring to form a homogeneous gel. The resulting synthesis gel had a molar composition of 0.5 Al_2O_3 : 12 SiO_2 : 5 NaOH : 3.57 TMAdaOH : 522 H_2O. The mixture was transferred into Teflon-lined autoclaves (45 mL, 4744, Parr Instrument) and subjected to hydrothermal crystallization at 160 °C for 96 h. After crystallization, the solid product was recovered by centrifugation, thoroughly washed with DI water, dried at 90 °C overnight, and finally calcined at 550 °C for 6 h.

The as-prepared SSZ-13 zeolite was ion exchanged to obtain its ammonium form (NH_4-SSZ-13). Specifically, 1 g of SSZ-13 was mixed with 1 g of NH_4NO_3 powder in 20 mL DI water and stirred at 95 °C for 2–3 h. The zeolite powder was then separated by centrifugation. This ion exchange procedure was repeated 3 times and then the samples were dried at 90 °C overnight to obtain NH_4-SSZ-13. To obtain pristine Cu-SSZ-13 zeolite, 1 g of the NH_4-SSZ-13 was dispersed in 100 mL 0.05 M $Cu(NO_3)_2$ (LP Chemicals Ltd) aqueous solution and stirred at room temperature (RT) for 24 h. The sample was subsequently recovered and washed 4 times by centrifugation using DI water. Finally, the sample was dried at 90 °C overnight and calcined at 550 °C for 6 h.

Impregnation is a commonly applied technique for studying the deactivation of Cu-SSZ-13 by various chemical species,[2] and it was adopted in this study to prepare alkali-poisoned catalysts. Specifically, 0.5 g of Cu-SSZ-13 powder was impregnated with 50 mL aqueous solutions of $NaNO_3$, KNO_3, NaCl and KCl at designated concentrations. The resulting slurry was dried at 80 °C for 24 h and subsequently calcined in air at 550 °C for 6 h. The prepared zeolite samples are denoted as $NaNO_3CuSSZ_x$, KNO_3CuSSZ_x, $NaClCuSSZ_x$ and $KClCuSSZ_x$, respectively, where x represents the nominal alkali content in them (mmol g_{catal}^{-1}). As a control, unpoisoned Cu-SSZ-13 samples were subjected to an identical treatment (using DI water without any salts) and calcination procedure, and the resulting sample was denoted as cCuSSZ.

2.2 Characterization of materials

XRD patterns of materials were collected using a PANaytical X'Pert Pro diffractometer, operating with Cu Kα1 radiation of 1.5406 Å at 40 kV and 40 mA. Data were recorded over a 2θ range of 5–50°, with a step increment of 0.03° s^{-1}. Crystallinity was determined *via* Gaussian peak deconvolution using Jade 9 software, calculated as the ratio of the summed intensity of crystalline peaks to the total intensity of both crystalline and

amorphous components.[19] Nitrogen (N_2) adsorption–desorption isotherms were obtained using a Micromeritics ASAP 2020 analyser. Samples were degassed under vacuum at 350 °C overnight prior to N_2 physisorption at −196 °C. The specific surface area (S_{BET}) and micropore volume ($V_{t\text{-plot}}$) were calculated using the Brunauer–Emmett–Teller (BET) and *t*-plot methods, respectively. XPS was performed on a Kratos AXIS Ultra DLD apparatus equipped with a monochromatized Al Kα radiation X-ray source. A charge neutraliser and a hemispherical electron energy analyser with a pass energy of 160 eV were employed. Binding energies (B.E.) were calibrated against the C 1s peak at 284.8 eV, and peak fitting was performed with G (30) type function and Tougard background. The instrument performance is routinely verified using Au and Ag standards. The charge neutraliser was used during the measurements. UV-vis spectra of the samples were recorded in the range of 200–1000 nm on a Shimadzu UV-2600 spectrophotometer in reflectance mode. Powdered samples were pressed into pellets and placed into a sample holder, with MgO was used as the reference. For electron paramagnetic resonance (EPR) measurements, approximately 10 mg of either ambient hydrated or fully dehydrated catalyst was loaded into the quartz EPR tube, and continuous scans of the sample were performed at 125 K. Catalyst dehydration was achieved by placing EPR tubes containing hydrated samples in a vacuum oven at 20 kPa and 250 °C for 3 h. The resulting spectra were double-integrated to determine signal areas, which are proportional to the amount of EPR-active isolated Cu^{2+} species. For quantification, calibration was performed using a series of standard solutions containing $Cu(NO_3)_2$ and imidazole dissolved in ethylene glycol.

H_2-TPR and NH_3-TPD analyses were performed using BELL-CAT II. For H_2-TPR, 100 mg of the sample was loaded in a quartz reactor and then pre-treated in air at 550 °C for 1 h. After cooling to RT, a flow of 0.5% H_2 in Ar was introduced into the reactor at flow rate of 50 mL min^{-1}. Once a stable hydrogen signal was detected on the thermal conductivity detector (TCD), system temperature was increased to 800 °C at 10 °C min^{-1}. For NH_3-TPD, 100 mg of sample was first pretreated at 550 °C in Ar (at 50 mL min^{-1}) for 1 h. The reactor was then cooled down to RT under Ar, after which a flow of 4% NH_3 in Ar (at 50 mL min^{-1}) was introduced into the reactor for 2 h to allow for NH_3 adsorption. Excess and weakly bound NH_3 was removed by purging with pure Ar for an additional hour. The desorption profiles were obtained by heating the catalysts from RT to 750 °C under Ar flow (at 50 mL min^{-1}) at a ramp rate of 10 °C min^{-1}.

FT-IR spectra were acquired using a Nicolet IS5 spectrometer. To investigate the OH stretching vibration region (OH-IR), catalyst samples (20 mg) were finely ground and pressed into self-supported wafers. These wafers were mounted in a vacuum cell (quartz composite *in situ* infrared transmission cell, QIRS-A03, Xiamen tuo-si Company, China). The samples were pretreated by heating to 400 °C under vacuum for 2 h, followed by cooling to RT prior to spectral acquisition. The Lewis and Brønsted acid sites of the catalysts were examined by the spectrometer above combined with pyridine adsorption/desorption (Py-IR). For this, 20 mg of each catalyst was pressed into a 13 mm dimeter self-supported wafer and placed in an IR quartz cell. The wafers were then activated at 350 °C for 2 h under high vacuum conditions ($<10^{-5}$ Pa) and subsequently cooled down to RT. Pyridine was introduced at ambient temperature (30 °C) and allowed to adsorb for 10 s to ensure saturation. Following adsorption, the system was evacuated at 200 °C to remove the physically adsorbed pyridine on the catalyst surface. FT-IR spectra were recorded in the 1600–1400 cm^{-1} range to characterize the chemisorbed pyridine species associated with Brønsted and Lewis acid sites.

2.3 Catalytic NH_3-SCR

Catalytic SCR experiments over the zeolitic catalysts were carried out in a fixed-bed quartz tubular reactor with an inner diameter of 6 mm under atmospheric conditions. Approximately 50 mg of pelletized catalyst, sieved to a particle size between 350 and 600 μm, were loaded into the reactor. The feed gas mixture consisted of 500 ppm NO, 500 ppm NH_3, 5% O_2 and 3% H_2O, balanced with Ar. The temperature was ramped from 100 °C to 650 °C at a rate of 10 °C min^{-1}, with isothermal holds of 30 minutes every 50 °C to ensure reaction equilibrium. The total flow rate was 200 mL min^{-1}, corresponding to a gas hourly space velocity (GHSV) of 190 000 h^{-1}. The outlet gas composition was analysed in-line by mass spectrometry (HPR-20 QIC, Hiden Analytical). NO conversion and N_2 selectivity were calculated using eqn (1) and (2), respectively.[20]

$$\text{NO conversion } (\%) = \frac{NO_{inlet} - NO_{outlet}}{NO_{inlet}} \times 100 \quad (1)$$

$$N_2 \text{ selectivity } (\%) = \frac{2N_{2outlet}}{NH_{3inlet} + NO_{inlet} - NH_{3outlet} - NO_{outlet}} \times 100\% \quad (2)$$

3. Results and discussion

3.1 Catalytic activity

NO conversion as a function of reaction temperature for both the pristine CuSSZ, cCuSSZ and alkali metal poisoned catalysts is presented in Fig. 1 and Fig. S1. The pristine CuSSZ and cCuSSZ catalyst exhibited consistently high NO_x conversions above 90% across a broad temperature window of 250–650 °C. In the low temperature region (100–200 °C), NO_x conversion increased sharply with rising temperature, from nearly 0% to approximately 80% at 200 °C. A slight decline in activity was observed at 650 °C, where NO_x conversion decreased marginally to 95%; nevertheless, this level of performance of cCuSSZ remained sufficiently high to ensure effective SCR operation.

Several common features were observed for the alkali metal poisoned catalysts. Notably, the presence of alkali metals slightly enhanced SCR activity below 250 °C, with an average increase of ~10% in NO_x conversion compared to cCuSSZ. This promotion was also reflected in lower apparent activation

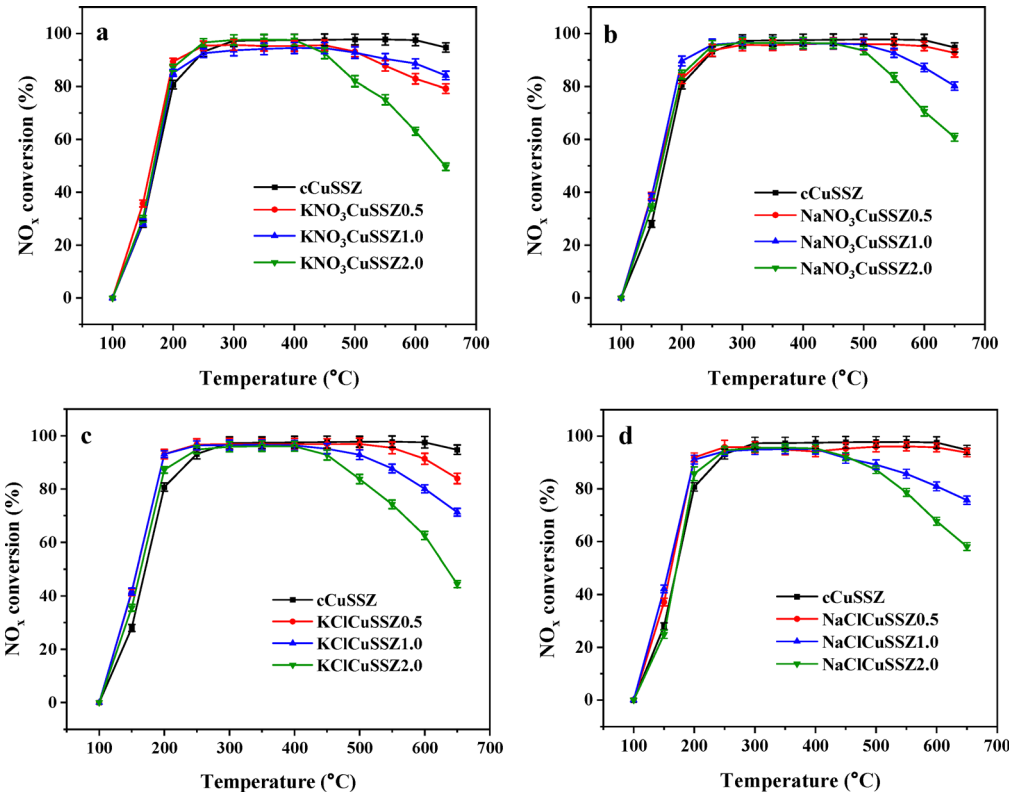

Fig. 1 Comparison of SCR activity of the pristine Cu-SSZ-13 catalyst (cCuSSZ) with the alkaline metal poisoned Cu-SSZ-13 catalysts: (a) KNO_3 poisoned catalysts, (b) $NaNO_3$ poisoned catalysts, (c) KCl poisoned catalysts and (d) NaCl poisoned catalysts. Reaction conditions: 500 ppm NO, 500 ppm NH_3, 5% O_2 and 3% H_2O in Ar balance; total flow rate: 200 mL min^{-1}; atmospheric pressure.

energies (Fig. S2). Conversely, pronounced deactivation occurred above 400 °C, with NO_x conversion decreasing by up to 50%. In the intermediate temperature range (250–400 °C), cCuSSZ exhibited slightly higher activity than the alkali metal poisoned samples. The low-temperature promotion effect decreased with increasing alkali metal loading. For example, NaClCuSSZ0.5 achieved 91.9% NO_x conversion at 200 °C, compared to 80.7% for cCuSSZ. Higher loadings led to reduced benefits: NaClCuSSZ1.0 reached 91.0%, and NaClCuSSZ2.0 only 85.7%. At high temperatures (>400 °C), the detrimental effect of alkali metals on SCR activity became more pronounced with increasing loading: NO_x conversions at 650 °C were 93.7%, 75.7%, and 58.1% for NaClCuSSZ0.5, NaClCuSSZ1.0, and NaClCuSSZ2.0, respectively.

Previous studies have reported similar low-temperature promotion of SCR activity by alkali metals. Cui *et al.*[21] observed that NO_x conversion below 200 °C increased with Na^+ or K^+ loading, peaking at Na/Cu or K/Cu ratios of ~0.7, beyond which activity declined. This enhancement was attributed to the stabilization of the SSZ-13 framework and repulsive interactions between Cu^{2+} ions and alkali metal cations, which prevented excessive Cu aggregation. Zhao *et al.*[10] further demonstrated *via* ^{27}Al and ^{1}H MAS NMR that Na^+ stabilizes framework Al, whereas excessive alkali metal loading promotes CuO_x formation, explaining the adverse effect on activity. Moreover, aggregation of isolated Cu species into CuO_x is accelerated at high temperatures, consistent with the severe deactivation observed above 400 °C.[22] H_2-TPR measurements confirmed that higher alkali metal contents accelerate this transformation.[11]

It is noteworthy that K-poisoning induces more severe deactivation of Cu-SSZ-13 at high temperatures than Na-poisoning. Under identical conditions, the T_{90} temperature window (range where NO_x conversion is >90%) is consistently narrower for K-poisoned samples. For example, KNO_3CuSSZ0.5 exhibits a T_{90} window of 250–500 °C, whereas $NaNO_3$CuSSZ0.5 maintains a broader range of 250–650 °C. Similarly, KClCuSSZ0.5 shows a T_{90} window of 200–600 °C compared to 200–650 °C for NaClCuSSZ0.5. Even when the T_{90} ranges are identical, as observed for KClCuSSZ2.0 and NaClCuSSZ2.0 (both 250–450 °C), the K-poisoned catalyst consistently delivers lower NO_x conversions at elevated temperatures; for example, NaClCuSSZ2.0 achieves 5–15% higher NO_x conversion than KClCuSSZ2.0 above 450 °C. This difference can be attributed to the stronger poisoning effect of K, which is more prone than Na to migrate into the chabazite (CHA) framework and exchanges with isolated Cu^{2+} ions. This behaviour arises from its smaller hydrated ionic radius (3.31 Å for K *vs.* 3.58 Å for Na) and stronger binding affinity to Cu-SSZ-13 acid sites (−6.0675 eV for K *vs.* −5.8929 eV for Na), ultimately leading to more pronounced catalyst deactivation.[2,23,24]

Alkali metal chlorides also exerted more pronounced deactivation than their nitrate counterparts, particularly at temperatures exceeding the T_{90} window. For instance, at >500 °C, NO_x

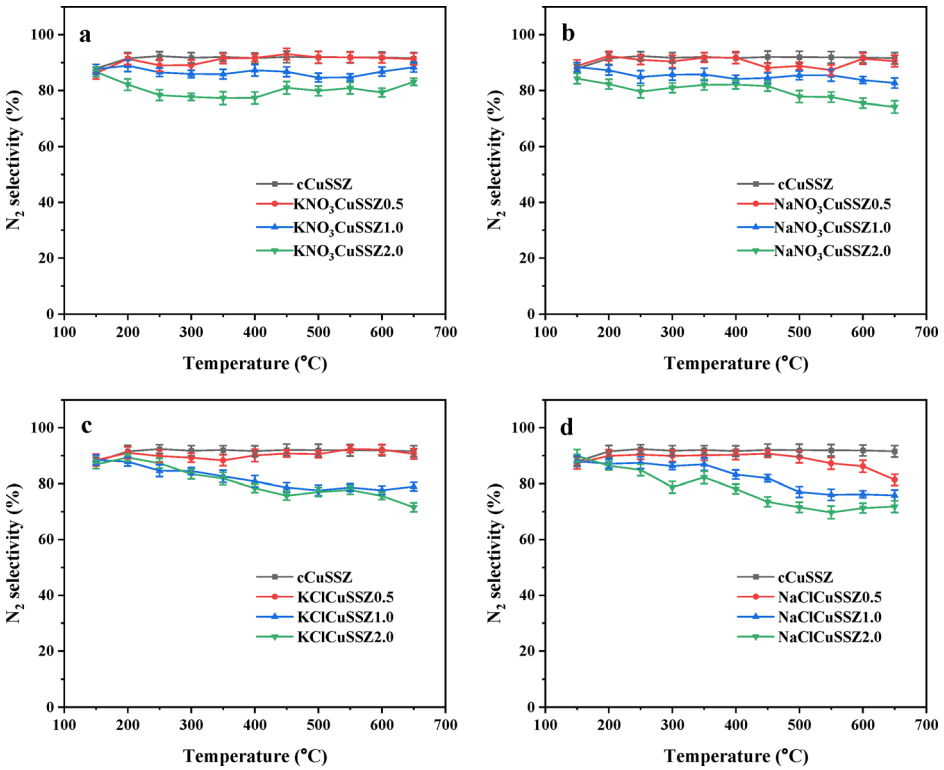

Fig. 2 Comparison of N_2 selectivity of the pristine cCuSSZ with the alkaline metal poisoned Cu-SSZ-13 catalysts: (a) KNO_3 poisoned catalysts, (b) $NaNO_3$ poisoned catalysts, (c) KCl poisoned catalysts and (d) NaCl poisoned catalysts. Reaction conditions: 500 ppm NO, 500 ppm NH_3, 5% O_2 and 3% H_2O in Ar balance; total flow rate: 200 mL min^{-1}; atmospheric pressure.

conversion over KCl-poisoned catalysts was typically 1–11% lower than that of KNO_3-poisoned catalysts at equivalent potassium loading. Sodium-containing catalysts showed a similar trend, with NaCl-poisoned samples displaying a 1–7% lower NO_x conversion than $NaNO_3$ analogues. This disparity became more pronounced at higher temperatures. For example, the difference in NO_x conversion between KClCuSSZ1.0 and KNO_3CuSSZ1.0 increased from 2.69% at 550 °C to 12.85% at 650 °C.

Fig. 2 presents the N_2 selectivity of cCuSSZ and alkali metal-poisoned catalysts. cCuSSZ maintained consistently high N_2 selectivity (~90%) across the entire temperature range of 150–600 °C. In contrast, the introduction of alkali metals reduced N_2 selectivity, with the effect becoming more pronounced at higher alkali metal loadings. For instance, KNO_3CuSSZ0.5 exhibited selectivity comparable to that of cCuSSZ, whereas KNO_3CuSSZ1.0 showed a 2–7% decrease relative to KNO_3-CuSSZ0.5, and KNO_3CuSSZ2.0 showed an additional 1–9% decline compared to KNO_3CuSSZ1.0. A similar trend was observed for other alkali metal poisoned catalysts, confirming the generality of this deactivation behaviour. In addition to alkali metal content, the counter anion also influenced N_2 selectivity, *i.e.*, alkali metal chlorides induced more pronounced deactivation than the corresponding nitrates. For example, KNO_3CuSSZ1.0 maintained N_2 selectivity above 80% over the entire temperature range, whereas KClCuSSZ1.0 dropped below 80% at temperatures above 400 °C.

The most substantial difference in NO_x conversion and N_2 selectivity between the nitrate- and chloride-poisoned catalysts was observed at an alkali metal loading of 1 mmol g_{catal}^{-1}, since this intermediate loading is sufficient to cause noticeable deactivation while avoiding the complete suppression observed at higher loading, thereby amplifying the contrast between nitrate and chloride poisoning. Specifically, at 650 °C, the NO_x conversion of KNO_3- and KCl-poisoned catalysts was 84.1% for KNO_3CuSSZ1.0 *vs.* 71.3% for KClCuSSZ1.0, compared with 79.2% for KNO_3CuSSZ0.5 *vs.* 84.0% for KClCuSSZ0.5 and 49.6% for KNO_3CuSSZ2.0 *vs.* 44.4% for KClCuSSZ2.0. A comparable trend was also found for sodium-poisoned samples as well. Therefore, comprehensive characterisation was conducted for KNO_3CuSSZ1.0, $NaNO_3$CuSSZ1.0, KClCuSSZ1.0, NaClCuSSZ1.0, and cCuSSZ to gain insights into the measured activity difference.

3.2 Characterization of crystalline and textural properties

To understand the underlying causes of catalytic deactivation induced by alkali metal poisoning, it is critical to assess whether the framework structure and porosity of the catalysts are preserved. Previous studies have shown that the collapse of the zeolite skeleton and the blockage of the zeolite pores can contribute to the inhibited SCR performance of Cu-SSZ-13 poisoned by alkali metals/alkaline earth metals.[23,25] Therefore, in this section, XRD and nitrogen physisorption analysis were

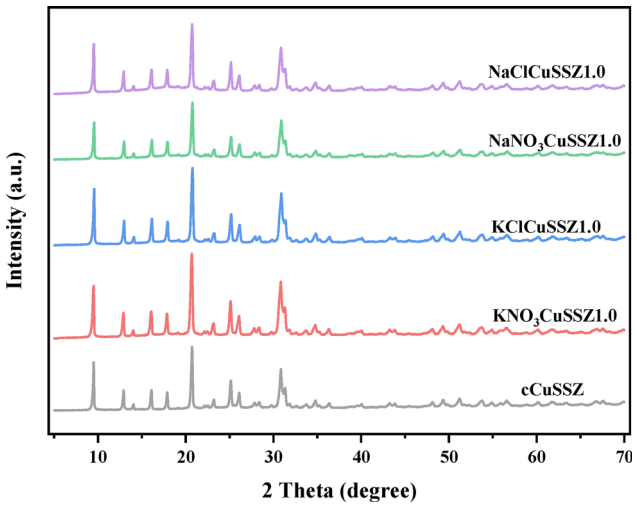

Fig. 3 XRD patterns for the cCuSSZ, KNO_3CuSSZ1.0, $NaNO_3$CuSSZ1.0, KClCuSSZ1.0, and NaClCuSSZ1.0 catalysts.

employed to examine the crystallinity and surface area of the catalysts after poisoning.

XRD patterns of the zeolitic materials (Fig. 3) show the characteristic diffraction peaks of the crystalline CHA phase at 2θ of 9.6°, 13.0°, 16.3°, 18.0°, 20.9° and 25.3°,[26,27] confirming the preservation of the CHA framework after impregnation using different alkali metal salts. However, compared to cCuSSZ, the crystallinity of the poisoned samples decreases (Table 1), and alkali metal chlorides cause greater loss in crystallinity than their nitrate counterparts. For example, the relative crystallinity of NaClCuSSZ1.0 is 89.2%, whilst it is 93.7% for $NaNO_3$CuSSZ1.0. A similar trend was observed in K-poisoned catalysts, where KClCuSSZ1.0 showed approximately 6% lower crystallinity than KNO_3CuSSZ1.0 (86.4% *vs.* 92.9%).

It is worth noting that diffraction peaks corresponding to copper oxide phases (*e.g.*, CuO or Cu_2O) were not detected by XRD, suggesting either highly dispersed Cu species or isolated Cu^{2+} ions at ion-exchange sites.[28] Also, diffraction features related to sodium- or potassium-containing phases were not observed, possibly due to their amorphous nature or low concentrations.[3] However, it should be noted that XRD lacks the sensitivity to detect highly dispersed Cu species or subtle changes in the Cu coordination environment, and thus cannot definitively rule out transformations of active Cu species.[29,30]

To investigate the effect on porosity, nitrogen physisorption analysis was conducted for the relevant samples here. The adsorption–desorption isotherms are shown in Fig. S3, exhibiting comparable type I isotherms for microporous materials according to the IUPAC classification.[31,32] The unusual slow N_2 uptake at high relative pressures in the isotherms is attributed to polarization-enhanced physisorption induced by Na^+ and K^+ in the pores or ion-exchange sites of the zeolites,[33] as well as the presence of framework defects or enlarged pores as suggested by Py-IR (Fig. 5a). The calculated values of S_{BET} and *t*-plot micropore volume ($V_{t\text{-plot}}$) are shown in Table 1. cCuSSZ exhibits an S_{BET} of 549 $m^2\ g^{-1}$ and $V_{t\text{-plot}}$ of 0.17 $cm^3\ g^{-1}$. After salt impregnation, the resulting catalysts show a slight decrease in S_{BET} and $V_{t\text{-plot}}$ (Table 1), likely due to the partial pore blockage or surface coverage by alkali metal species and the declined structural integrity. These changes may hinder the adsorption of reactant molecules, thereby contributing to SCR deactivation.[23,25]

Table 1 Structural and textural properties of the pristine and alkali metal poisoned SSZ-13 zeolites

Samples	S_{BET} ($m^2\ g^{-1}$)	$V_{t\text{-plot}}$ ($cm^3\ g^{-1}$)	Crystallinity (%)
cCuSSZ	549	0.17	100
KNO_3CuSSZ1.0	521	0.15	92.9
$NaNO_3$CuSSZ1.0	522	0.16	93.7
KClCuSSZ1.0	500	0.16	86.4
NaClCuSSZ1.0	525	0.15	89.2

3.3 Characterization of acidic properties

Catalyst acidity plays a significant role in SCR reactions. Specifically, the active isolated Cu^{2+} species are the primary source of Lewis acid sites in the catalysts, while Brønsted acid sites primarily serve as the reservoir concentrating local NH_3 near active Cu-ion species and thereby facilitating the SCR reaction.[34] The detrimental effects of alkali metal poisoning on the acidity of SCR catalysts have been reported in V-based, Mn-based and zeolite-based systems.[2,3,35–38] Therefore, NH_3-TPD, Py-IR and OH-IR were employed in this study to evaluate the change in acidic properties of the catalysts. Changes in acidic properties of Cu-SSZ-13 due to alkali metal poisoning were firstly probed by NH_3-TPD (Fig. 4). The NH_3-TPD profile of cCuSSZ could be deconvoluted into three desorption peaks, in agreement with the findings in previous studies.[39,40] The low-temperature desorption peak (LT peak, centered at ~170 °C) is attributed to physisorbed NH_3 and weakly adsorbed NH_3 on weak Lewis acid sites, such as extra-framework Al species.[41–43] The medium-temperature peak (MT peak, centered at ~310 °C) corresponds to NH_3 desorption from stronger Lewis acid sites, primarily associated with Cu^{2+} ions.[44] To confirm the MT peak originating from Cu^{2+} sites and not being influenced by the presence of alkali metal salts, NH_3-TPD analyses were also conducted for alkali metal loaded NH_4-SSZ-13 samples (Fig. S4). The corresponding profiles show no MT peaks, which supports the assignment of the MT peak exclusively to Cu^{2+} species. The high-temperature peak (HT peak, centered at ~500 °C) can be ascribed to NH_3 desorption from strong Brønsted acid sites in the zeolite.[45] In the profiles of the poisoned zeolite catalysts, an additional desorption peak appeared at around 120 °C, which is attributed to NH_3 weakly adsorbed on alkali metal cations (K^+ and Na^+ sites).[24,46]

Based on the deconvolution, concentrations of different acid sites are quantified (Table 2). Compared with cCuSSZ, the alkali metal poisoned samples exhibited a shift of the LT peak toward lower temperatures, accompanied by reduced intensities. This behaviour can be ascribed to the stronger affinity of alkali metal ions for NH_3 adsorption, which weakens the interaction of NH_3 with physisorption sites and extra-framework Al species.[47]

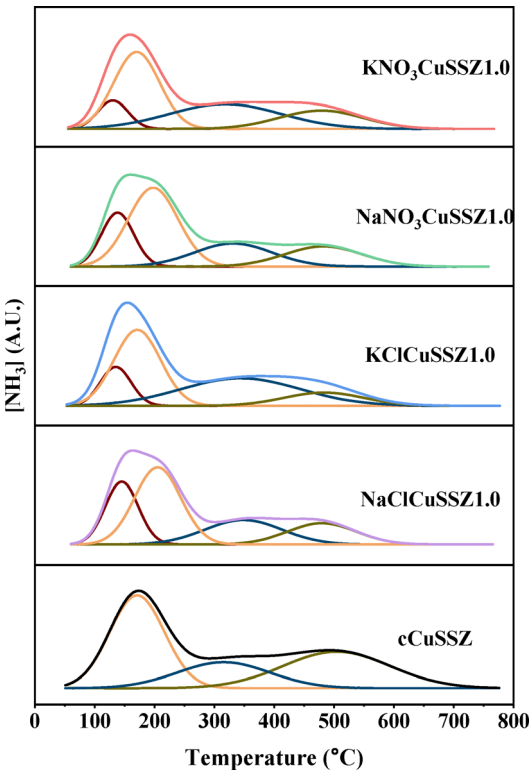

Fig. 4 NH_3-TPD profiles of the cCuSSZ, KNO_3CuSSZ1.0, $NaNO_3$-CuSSZ1.0, KClCuSSZ1.0, and NaClCuSSZ1.0 catalysts.

Similar observations have been reported previously.[12,25,48] Additionally, the alkali metal poisoning caused a decrease in Brønsted acidity and strong Lewis acidity of the resulting zeolite catalysts, which is primarily attributed to the replacement of H^+ in Brønsted acid sites (Si–O(H)–Al) and ion-exchanged Cu^{2+} sites by alkali metal ions.[24] It is worth noting that Brønsted acid sites are more severely affected by alkali metal poisoning than Cu^{2+}-associated Lewis acid sites. In specific, in comparison with cCuSSZ, the amount of NH_3 desorbed from Brønsted acid sites in NaClCuSSZ1.0, KClCuSSZ1.0, $NaNO_3$CuSSZ1.0 and KNO_3CuSSZ1.0 decreased by 31.4%, 40.4%, 30.6%, and 33.2%, respectively. Conversely, the amounts of NH_3 desorbed from Cu^{2+} ions within the zeolitic catalysts were better retained, as shown in Table 2. Hence, the findings so far suggest that Brønsted acid sites are more susceptible to alkali metal poisoning than Cu^{2+} sites, in agreement with previous studies on alkali metal-induced deactivation in zeolite catalysts.[3,49]

To explicitly identify the surface acidic nature of the catalysts, quantitative analysis of the Brønsted and Lewis acid sites was conducted using Py-IR. Fig. 5a shows that all the catalysts exhibited the characteristic absorption bands at approximately 1450, 1490, and 1540 cm^{-1}. The band at 1450 cm^{-1} is attributed to pyridine coordinated to Lewis acid sites, whilst the band at 1540 cm^{-1} corresponds to pyridine coordinated to Brønsted acid sites.[50,51] The band at 1490 cm^{-1} is commonly ascribed to the combined contribution from both Brønsted and Lewis acid sites.[52] Concentrations of Brønsted/Lewis acid sites were quantified from the integrated absorbance of the respective IR bands, with the results summarized in Table 2. Overall, the alkali metal chlorides exerted a stronger detrimental effect on acidity in Cu-SSZ-13 than their nitrate counterparts. For example, relative to cCuSSZ, the Brønsted acid concentration decreased by 4.7% for $NaNO_3$CuSSZ1.0 and by 21% for NaClCuSSZ1.0, while KNO_3CuSSZ1.0 and KClCuSSZ1.0 showed decreases by 0.9% and 16.5%, respectively. However, the decline in Brønsted acidity detected by Py-IR was less pronounced than that indicated by NH_3-TPD. This discrepancy likely arises from the relatively large kinetic diameter of pyridine (0.58 nm), which restricts its diffusion into the microporous CHA framework of SSZ-13 (0.38 nm).[53] Nevertheless, the presence of detectable Py-IR signals suggests that a fraction of the acid sites is located in more accessible environments, such as pore mouths and enlarged framework defects, where pyridine molecules can adsorb. These same accessible environments may also interact with N_2 molecules at high relative pressures, thereby providing a plausible explanation for the unusually slow uptake observed in the adsorption (Fig. S3).

To assess the impact of alkali metal poisoning on Brønsted acidity within the bulk of Cu-SSZ-13, FT-IR spectra in the OH stretching vibration region were analysed (Fig. 5b). cCuSSZ exhibited two distinct OH stretching bands at ~3610 and ~3732 cm^{-1}, attributed to Brønsted acid sites (Si–OH–Al groups within the zeolite framework) and terminal silanol groups on the external surface, respectively.[54,55] Upon alkali metal poisoning, two additional peaks appeared at 3660 and 3707 cm^{-1}, corresponding to silanol defects formed *via*

Table 2 Acidic properties of fresh and alkali metal poisoned zeolite catalysts

Sample	NH_3 desorption[a] (μmol g^{-1})			Brønsted acid concentration[b] (μmol g^{-1})	Lewis acid concentration[b] (μmol g^{-1})	Peak intensity[c] (—)
	LT peak	MT peak	HT peak			
cCuSSZ	66.1	45.8	58.6	67.1	25.2	51.3
$NaNO_3$CuSSZ1.0	70.3	32.2	28	63.9	35.4	40.4
KNO_3CuSSZ1.0	57.9	45.4	25.4	66.5	25	36.7
NaClCuSSZ1.0	66.5	35.2	27.2	53	18.1	35.5
KClCuSSZ1.0	60.8	56.7	18.2	56	16.9	31.3

[a] NH_3 desorption amounts from LT, MT, and HT peaks were quantified based on the NH_3-TPD results (Fig. 4). [b] Brønsted and Lewis acid concentrations were determined from the Py-IR spectra (Fig. 5a). [c] Peak intensities of the 3610 cm^{-1} band were determined from the OH-IR spectra (Fig. 5b).

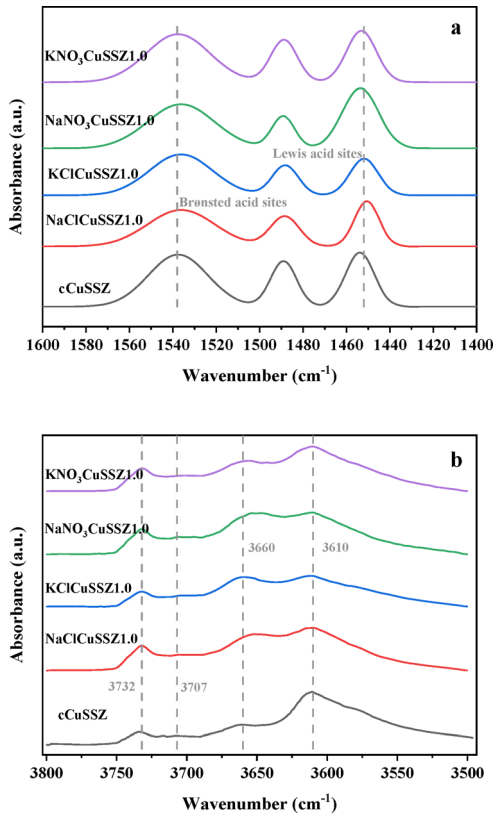

Fig. 5 (a) Py-IR spectra and (b) OH-IR spectra of the cCuSSZ, KNO_3-CuSSZ1.0, $NaNO_3$CuSSZ1.0, KClCuSSZ1.0, and NaClCuSSZ1.0 catalysts.

framework dealumination,[54] consistent with the reduction in crystallinity observed *via* XRD (Fig. 3). The relative Brønsted OH content was evaluated from the integrated intensity of the 3610 cm^{-1} band. Quantitative analysis revealed a 21–39% decrease in the intensity among the poisoned samples, aligning closely with the ~30% reduction in Brønsted acidity estimated by NH_3-TPD (Fig. 4). Among these, $NaNO_3$CuSSZ1.0 showed the smallest decrease (21.2%), whereas KClCuSSZ1.0 exhibited the largest decline (40.0%). These findings confirm that alkali metal chlorides, particularly potassium chloride, impose a markedly stronger detrimental effect on Brønsted acidity in Cu-SSZ-13 compared to the nitrate counterparts.

The findings above demonstrate that the Brønsted acid sites in Cu-SSZ-13 are particularly susceptible to being affected by alkali metal poisoning. During NH_3-SCR, these sites primarily serve as the reservoir concentrating local NH_3 near active Cu-ion species and thereby facilitating the SCR reaction.[34] Thus, synergistic interactions between Brønsted acid sites and active Cu ions can significantly influence SCR activity *via* enhanced sorption stability and/or transition-state stabilization.[56] Notably, the decline in Brønsted acidity mirrors the reduction in SCR activity, with catalysts poisoned by potassium and alkali metal chlorides exhibiting the most substantial activity losses. These findings suggest that the degradation of Brønsted acid sites is a key contributor to the deactivation of Cu-SSZ-13 due to alkali metal poisoning.

3.4 Characterization of redox properties and Cu species transformation

Findings on the changes in acidity suggest a loss of isolated Cu^{2+} species after impregnation of alkali metals. To distinguish between different types of isolated Cu^{2+} species (*i.e.*, $ZCu^{II}OH$ and Z_2Cu^{II}) and reveal the transformation of these species, H_2-TPR, EPR, UV-vis spectroscopy and XPS were employed to provide further insights into the reducibility, coordination environments and oxidation states of Cu species. H_2-TPR characterization was conducted firstly to distinguish between the two types of isolated Cu^{2+} species present in the catalysts and evaluate the poisoning-induced effect on them (Fig. 6). To determine the effect of alkali metal salts and the SSZ-13 framework, H_2-TPR analyses were first performed on alkali metal loaded NH_4-SSZ-13 samples. As shown in Fig. S5, no reduction peaks were observed for the control samples, confirming that the impregnated alkali metal species and the SSZ-13 zeolite contribute negligibly to the reduction process.[3] For the Cu-containing catalysts under investigation, they show two characteristic reduction peaks at approximately 240 °C and 360 °C, corresponding to the reduction of Cu species located in 8-membered rings ($ZCu^{II}OH$) and 6-membered rings (Z_2Cu^{II}), respectively.[57–59] Compared to cCuSSZ, the alkali metal poisoned samples showed enhanced peak intensities at 240 °C (5% to 76% enhancement) and reduced peak intensities at 360 °C (19% to 93% reduction). This trend suggests the

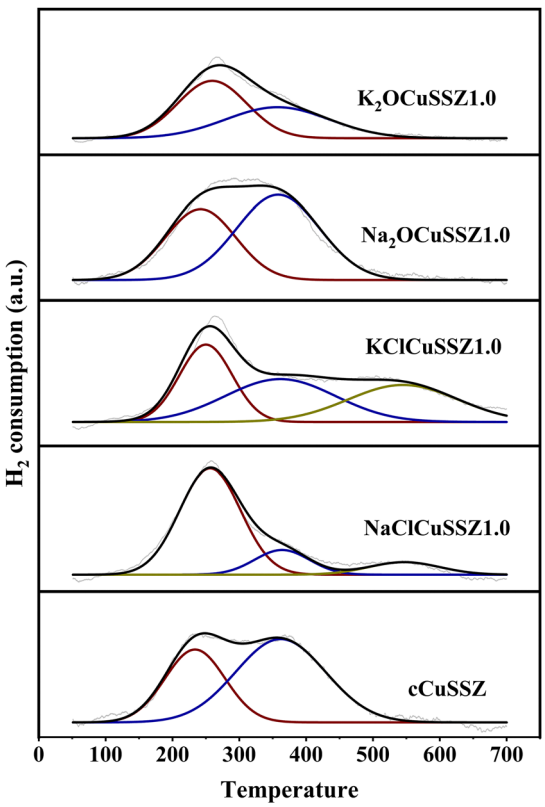

Fig. 6 H_2-TPR profiles of the cCuSSZ, KNO_3CuSSZ1.0, $NaNO_3$CuSSZ1.0, KClCuSSZ1.0, and NaClCuSSZ1.0 catalysts.

transformation of Z_2Cu^{II} into $ZCu^{II}OH$ upon alkali metal poisoning. Additionally, a third reduction peak was observed at around 545 °C in NaClCuSSZ1.0 and KClCuSSZ1.0 samples, which was assigned to the reduction of $CuAlO_x$ species.[60,61] These species are commonly described as disordered $CuAl_2O_4$-like phases or Al-rich CuO_x clusters.[62,63]

Since Cu^+ ions and CuO_x species are EPR silent, the isolated Cu(II) species (Z_2Cu^{II} in 6 MR and $ZCu^{II}OH$ in 8 MR) can be selectively quantified by EPR.[59,64] Previous studies have shown that both fully hydrated Z_2Cu^{II} and $ZCu^{II}OH$ are EPR active; however, upon dehydration, only Z_2Cu^{II} remains detectable by EPR.[64,65] In contrast, $ZCu^{II}OH$ becomes EPR silent *via* three possible pathways: (i) autoreduction to Cu^+-Z species, which are EPR silent due to the absence of unpaired electrons; (ii) condensation to multinuclear Cu species, which are EPR silent due to antiferromagnetic coupling; and (iii) dehydration to a $[Cu(OH)]^+$ species with a planar three-coordination, rendered EPR silent due to a pseudo Jahn–Teller effect.[21] Exploiting this difference, the relative concentrations of Z_2Cu^{II} and $ZCu^{II}OH$ can be quantified by comparing EPR spectra of hydrated and dehydrated samples (Fig. S6). The quantification results (Fig. 7) are in good agreement with the H_2-TPR results, indicating that alkali metal poisoning promotes the transformation of Z_2Cu^{II} to $ZCu^{II}OH$, with an observed increase of 5–17% in $ZCu^{II}OH$ content. Furthermore, the concurrent decrease in the total number of Cu^{2+} species suggests that a fraction of Z_2Cu^{II} is additionally transformed into EPR-silent species such as CuO_x upon alkali metal poisoning.

The generation of $CuAlO_x$ species suggests the likely transformation of isolated Cu^{2+} species into CuO_x due to the poisoning, though CuO_x species were not detected by H_2-TPR. Therefore, UV-vis spectroscopy was employed to detect the possible presence of CuO_x species in the poisoned catalysts. To isolate the spectral contributions of Cu species, the spectra of alkali metal-poisoned NH_4-SSZ-13 samples were subtracted as baselines, eliminating the influence of alkali metals and the parent zeolite framework. A prominent absorption band at approximately 220 nm is attributed to oxygen-to-metal charge transfer related to the isolated Cu^{2+} bound on the framework of zeolite.[66,67] The 400–600 nm region can be employed as an indicator for the presence of copper oxides, as CuO_x species exhibit strong absorption in this region, whereas Cu^{2+} ions and $Cu(OH)_2$ do not.[68,69] Broad absorption features observed between 600 and 800 nm correspond to the electron d–d transitions of Cu^{2+} with a hexacoordinated octahedral structure.[70–72] Compared to fresh Cu-SSZ-13 catalyst, all alkali metal-poisoned samples exhibit a decrease in the intensity of the 220 nm band and an increase in absorption within the 400–600 nm region, suggesting the transformation of isolated Cu^{2+} ions to CuO_x species. Notably, in NaClCuSSZ1.0 and KClCuSSZ1.0, an additional absorption peak emerges at approximately 275 nm, which is assigned to square-planar Cu oxide clusters (the precursors of the highly dispersed copper oxide phase).[29] The occurrence of dealumination (confirmed by XRD, Fig. 3) and the presence of this species account for the formation of $CuAlO_x$ species as detected in H_2-TPR profiles (Fig. 6).

The distinction between isolated Cu^{2+} species and CuO_x species after alkali metal poisoning was further investigated using XPS (Fig. 9). All spectra exhibit characteristic Cu 2p signals with board main peaks corresponding to Cu $2p_{3/2}$ and Cu $2p_{1/2}$. The Cu $2p_{3/2}$ envelop was deconvoluted into two distinct components with binding energies (B.E.) in the range of 933.1–933.4 eV and 935.4–937.1 eV (Table S1). According to the literature, Cu species with B.E. $<$ 930.0 eV are assigned to metallic copper (Cu^0), which was not detected in any samples, while peaks above 933.0 eV are typically attributed to cupric species, including isolated Cu^{2+} and CuO_x species.[18,71,73] Notably, isolated Cu^{2+} species exhibit higher B.E. than CuO_x, enabling their distinction.

On this basis, the peak at 933.3–933.6 eV was assigned to CuO_x, whereas the higher B.E. peak at 936.7–936.9 eV was assigned to isolated Cu^{2+} species. The relative proportions of isolated Cu^{2+} and CuO_x species were quantified from the integrated peak areas. Interestingly, the observed B.E. values for Cu ions in our samples are higher than those of bulk Cu compounds, suggesting that Cu species are predominantly stabilized in ion-exchange positions within the zeolite framework rather than as external aggregates.[74] Among all the catalysts, the pristine cCuSSZ catalyst exhibited the highest surface concentration of the isolated Cu^{2+} species (~17.6%), while significantly lower values were observed for the alkali-metal-poisoned samples (10.1%, 12.1%, 10.1% and 9.69%, Fig. S7). This confirms that alkali metal loading decreases the population of catalytically active isolated Cu^{2+} ions. These findings are consistent with the trends observed in NH_3-TPD (Fig. 4), EPR (Fig. 7), UV-vis (Fig. 8) and catalytic performance (Fig. 1). Furthermore, the pristine cCuSSZ also exhibited the highest B.E. for isolated Cu^{2+} species (937.04 eV), compared to that of the poisoned samples (Table S1). This further supports that the Cu ions in the pristine cCuSSZ catalysts are more

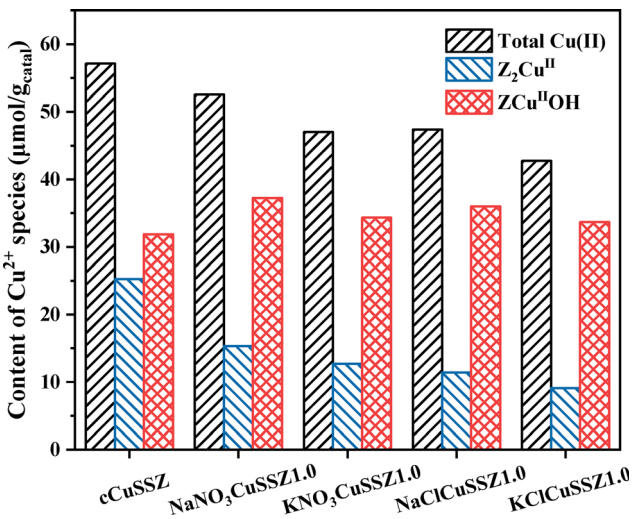

Fig. 7 Content of different Cu^{2+} species by EPR for cCuSSZ, KNO_3-CuSSZ1.0, $NaNO_3$CuSSZ1.0, KClCuSSZ1.0, and NaClCuSSZ1.0 catalysts.

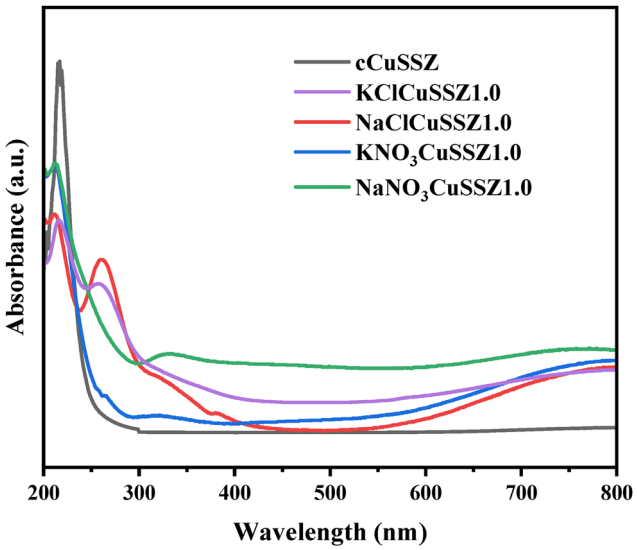

Fig. 8 UV-vis spectra of the cCuSSZ, KNO_3CuSSZ1.0, $NaNO_3$CuSSZ1.0, KClCuSSZ1.0, and NaClCuSSZ1.0 catalysts.

uniformly dispersed within the zeolite framework, rather than forming aggregates like in the alkali metal poisoned catalysts.[74]

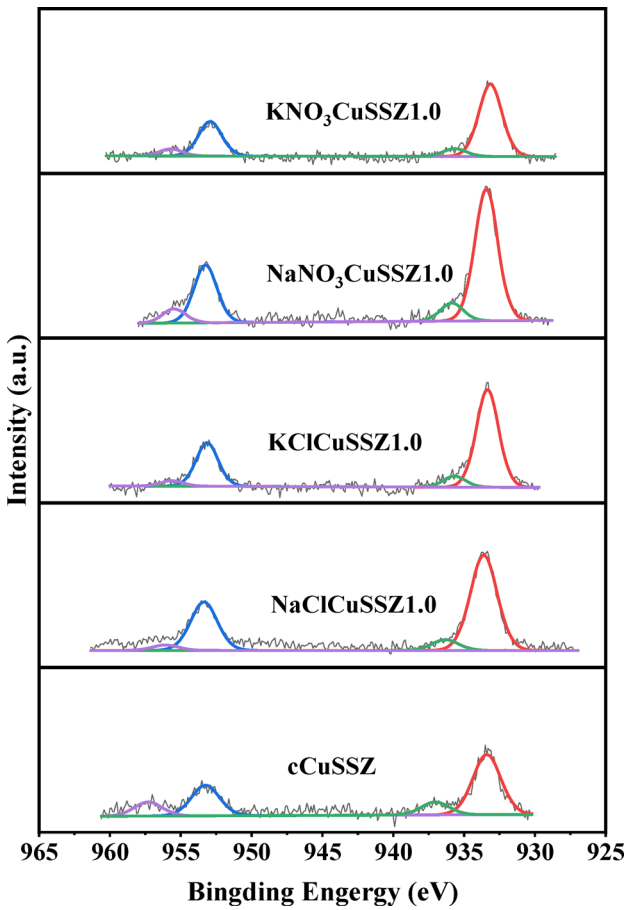

Fig. 9 XPS spectra of Cu 2p regions for the cCuSSZ, KNO_3CuSSZ1.0, $NaNO_3$CuSSZ1.0, KClCuSSZ1.0, and NaClCuSSZ1.0 catalysts.

The results above confirm that alkali metal poisoning induces a transformation of Cu species within the zeolite framework. Two possible pathways are proposed to explain these changes: (i) a portion of the Z_2Cu^{II} originally located at 6MR may be converted into $ZCu^{II}OH$ at 8MR due to the competitive adsorption between alkali cations and Cu^{2+}, contributing to the enhanced low-temperature catalytic activity observed in the alkali metal poisoned samples; and (ii) another portion of Z_2Cu^{II} is transformed into CuO_x species, and in the case of alkali metal chloride poisoning, these CuO_x species interact with extra-framework aluminium species to form $CuAlO_x$ species. This transformation is associated with a decline in high-temperature catalytic performance.

The generation of $CuAlO_x$ species in alkali metal chloride poisoned samples is supported by the findings by H_2-TPR (Fig. 6), although distinguishing $CuAlO_x$ species from CuO_x species based on UV-vis spectra and XPS spectra remains challenging. The difficulty arises due to the similar oxidation states and coordination geometries of Cu in both species. For example, both CuO_x and $CuAlO_x$ may adopt a hexacoordinated octahedral structure and contribute to the adsorption bands in the 600–800 nm range in UV-vis spectra, leading to overlapping. The formation of $CuAlO_x$ likely requires the involvement of two precursors: square-planar Cu oxide clusters and the aluminium hydroxide units generated *via* framework dealumination. In the samples poisoned by alkali metal nitrates, the absence of detectable square-planar Cu oxide clusters (Fig. 8) and the slight dealumination (Fig. 3) may explain the lack of $CuAlO_x$-associated reduction peaks in their H_2-TPR profiles (Fig. 6).

3.5. Property–activity relationship

Compared to the cCuSSZ catalyst, the poisoned samples exhibited slightly enhanced low-temperature activity (below 250 °C), but suffered from significant deactivation at high temperatures (above 400 °C). Notably, alkali metal chlorides induced more severe deactivation than their nitrate counterparts. These contrasting behaviours can be rationalized by considering changes in Cu speciation, catalyst acidity, and framework stability. The enhancement at low temperatures is primarily attributed to the transformation of Z_2Cu^{II} species to $ZCu^{II}OH$ species upon alkali metal poisoning, as $ZCu^{II}OH$ is known to exhibit superior SCR activity in this regime.[75,76] While some studies have suggested that moderate alkali metal addition may suppress framework dealumination and thereby improve activity,[10,21] our results show that dealumination occurs upon alkali metal loading. Thus, the transformation of Z_2Cu^{II} to $ZCu^{II}OH$ is proposed to be the dominant factor responsible for the observed promotion at low temperatures.

In contrast, the pronounced loss of high-temperature activity can be attributed to two main effects. First, alkali metal poisoning significantly reduces catalyst acidity. A ~30% decrease in Brønsted acidity was observed, and since Brønsted sites enhance local NH_3 concentration and facilitate SCR over neighbouring Cu species *via* sorption-enhanced catalysis and/or transition-state stabilization,[34,56] their depletion directly correlates with diminished activity. This decline is particularly

severe in chloride-poisoned catalysts, especially those containing KCl.

Second, the poisoning leads to depletion of isolated Cu^{2+} species, accompanied by the formation of inactive CuO_x and $CuAlO_x$ phases. Characterization revealed that $CuAlO_x$ features were present exclusively in NaClCuSSZ1.0 and KClCuSSZ1.0, implicating their formation as a major contributor to the stronger deactivation induced by chlorides. The intensified loss of isolated Cu^{2+} species in chloride-poisoned samples is further supported by their lower N_2 selectivity, since the emergence of CuO_x and $CuAlO_x$ species favours side reactions such as NH_3 oxidation, thereby reducing N_2 yield.[23,77]

The more severe deactivation in alkali metal chloride poisoned catalysts can be attributed to a synergetic effect between framework dealumination and transformation of isolated Cu^{2+} species. Due to its smaller Pauling radius and stronger nucleophilicity, Cl^- interacts more readily with the zeolite framework, thereby promoting dealumination at elevated temperatures.[78,79] The removal of framework Al reduces the number of negatively charged ion-exchange sites responsible for stabilizing Cu^{2+} species in SSZ-13. As a result, the anchoring strength of isolated Cu^{2+} is diminished, making them more prone to migrate and aggregate into CuO_x clusters.[61] Song *et al.* have similarly reported that CuO_x clusters readily migrate and aggregate at high temperatures, causing micropore damage and modifying zeolite porosity.[65] The formation of CuO_x species can further destabilize the zeolite cages, ultimately triggering partial framework collapse[80] and leading to the accumulation of detached Al hydroxide units and square-planar Cu oxide clusters (as evidenced by UV-vis, Fig. 8). These processes collectively result in the generation of $CuAlO_x$ species in chloride-poisoned samples. By contrast, NO_3^- anions possess a larger ionic radius and weaker nucleophilicity, which limit its interaction with the framework. Consequently, dealumination is negligible in nitrate-poisoned catalysts, and the depletion of isolated Cu^{2+} species occurs primarily *via* simple ion exchange with alkali cations, without significant $CuAlO_x$ formation. This mechanistic distinction explains the comparatively milder deactivation of nitrate-poisoned samples.

4. Conclusions

This study systematically investigated the effects of alkali metal salts (KCl, NaCl, KNO_3, and $NaNO_3$) on the NH_3-SCR performance of Cu-SSZ-13. Introduction of alkali metals (by impregnation) onto the zeolite slightly enhanced the low-temperature (<250 °C) catalytic activity, primarily through the transformation of Z_2Cu^{II} species into $ZCu^{II}OH$ species, resulting in up to $\sim$10% improvement in NO_x conversion. However, this promotion diminished with an increase in alkali metal loading. At higher temperatures (>400 °C), severe deactivation (up to 50%) was observed, driven by the depletion of isolated Cu^{2+} species and the loss in total acidity, particularly Brønsted acid sites. Among the tested salts, chlorides induced more pronounced deactivation than nitrates, attributable to a synergistic interplay between framework dealumination and Cu^{2+} (isolated) transformation, which together promote the accumulation of detached aluminium hydroxide units and square-planar Cu oxide clusters, ultimately leading to the formation of inactive $CuAlO_x$ species. These findings highlight the importance of minimizing alkali metal contamination, especially chloride, in practical SCR systems to ensure long-term stability and maintain high catalytic performance under industrial operating conditions.

Conflicts of interest

There are no conflicts to declare.

Data availability

Data for this article are available at the University of Manchester repository, Figshare at **https://doi.org/10.48420/30048292**.

Supplementary information (SI) is available. The supplementary information contains additional experimental details, characterization data and supporting figures. See DOI: **https://doi.org/10.1039/d5cp03404c**.

Acknowledgements

This project has received funding from the European Union's Horizon 2020 research and innovation programme under grant agreement No. 872102. This project is also supported by the National Natural Science Foundation of China (no. 22378407 and W2431016) for research and collaboration. B. W. and Y. Z. acknowledge the financial support from the China Scholarship Council (file no. 202106100037 and 202006100040) and the University of Manchester for supporting their PhD research.

References

1 J. Wang, H. Zhao, G. Haller and Y. Li, *Appl. Catal., B*, 2017, **202**, 346–354.
2 C. Wang, W. Yan, Z. Wang, Z. Chen, J. Wang, J. Wang, J. Wang, M. Shen and X. Kang, *Catal. Today*, 2020, **355**, 482–492.
3 L. Liu, X. Wu, Y. Ma, X. Zhang, R. Ran, Z. Si and D. Weng, *Chem. Eng. J.*, 2020, **383**, 123080.
4 J. Li, H. Chang, L. Ma, J. Hao and R. T. Yang, *Catal. Today*, 2011, **175**, 147–156.
5 L. Pang, C. Fan, L. Shao, K. Song, J. Yi, X. Cai, J. Wang, M. Kang and T. Li, *Chem. Eng. J.*, 2014, **253**, 394–401.
6 S. Zhang, L. Pang, Z. Chen, S. Ming, Y. Dong, Q. Liu, P. Liu, W. Cai and T. Li, *Appl. Catal., A*, 2020, **607**, 117855.
7 M. Klimczak, P. Kern, T. Heinzelmann, M. Lucas and P. Claus, *Appl. Catal., B*, 2010, **95**, 39–47.
8 I. Lezcano-Gonzalez, U. Deka, H. E. van der Bij, P. Paalanen, B. Arstad, B. M. Weckhuysen and A. M. Beale, *Appl. Catal., B*, 2014, **154–155**, 339–349.
9 L. Lisi and S. Cimino, *Catalysts*, 2020, **10**, 1475.

10 Z. Zhao, R. Yu, R. Zhao, C. Shi, H. Gies, F.-S. Xiao, D. De Vos, T. Yokoi, X. Bao, U. Kolb, M. Feyen, R. McGuire, S. Maurer, A. Moini, U. Müller and W. Zhang, *Appl. Catal., B*, 2017, **217**, 421–428.
11 L. Xie, F. Liu, X. Shi, F.-S. Xiao and H. He, *Appl. Catal., B*, 2015, **179**, 206–212.
12 C. Fan, Z. Chen, L. Pang, S. Ming, C. Dong, K. Brou Albert, P. Liu, J. Wang, D. Zhu, H. Chen and T. Li, *Chem. Eng. J.*, 2018, **334**, 344–354.
13 Y. Liu, L. Cheng, Y. Zhao, J. Ji, Q. Wang, Z. Luo and Y. Bai, *Fuel Process. Technol.*, 2018, **169**, 288–294.
14 H. Oleschko, A. Schimrosczyk, H. Lippert and M. Muller, *Fuel*, 2007, **86**, 2275–2282.
15 J. Cao, C. Nannuzzi, W. Liu, H. Wu, Y. Gao, R. Zhong, Q. Liu and G. Berlier, *Fuel*, 2022, **328**, 125262.
16 M. Kong, Q. Liu, J. Zhou, L. Jiang, Y. Tian, J. Yang, S. Ren and J. Li, *Chem. Eng. J.*, 2018, **348**, 637–643.
17 X. Du, G. Yang, Y. Chen, J. Ran and L. Zhang, *Appl. Surf. Sci.*, 2017, **392**, 162–168.
18 M. Chen, J. Li, W. Xue, S. Wang, J. Han, Y. Wei, D. Mei, Y. Li and J. Yu, *J. Am. Chem. Soc.*, 2022, **144**, 12816–12824.
19 M. Doumeng, L. Makhlouf, F. Berthet, O. Marsan, K. Delbé, J. Denape and F. Chabert, *Polym. Test.*, 2021, **93**, 106878.
20 F. Gao, X. Tang, H. Yi, S. Zhao, J. Wang and T. Gu, *Appl. Surf. Sci.*, 2019, **466**, 411–424.
21 Y. Cui, Y. Wang, D. Mei, E. D. Walter, N. M. Washton, J. D. Holladay, Y. Wang, J. Szanyi, C. H. F. Peden and F. Gao, *J. Catal.*, 2019, **378**, 363–375.
22 B. Wang, Y. Zhang and X. Fan, *Chem. Phys. Impact.*, 2023, **6**, 100207.
23 J. Zhou, B. Guan, J. Guo, J. Chen, Z. Liu, C. Zheng, T. Su, Y. Zhang, Y. Yuan, H. Dang, B. Xu, C. Xu, W. Zeng and Z. Huang, *Catal. Lett.*, 2023, **154**, 2761–2776.
24 F. Gao, Y. Wang, N. M. Washton, M. Kollár, J. Szanyi and C. H. F. Peden, *ACS Catal.*, 2015, **5**, 6780–6791.
25 B. Guan, J. Chen, J. Guo, Z. Liu, C. Zheng, J. Zhou, T. Su, Y. Zhang, Y. Yuan, H. Dang, B. Xu, C. Xu, W. Zeng and Z. Huang, *Ind. Eng. Chem. Res.*, 2023, **62**, 9662–9672.
26 J. Wang, L. Shao, C. Wang, J. Wang, M. Shen and W. Li, *J. Catal.*, 2018, **367**, 221–228.
27 J. Wang, Z. Peng, Y. Chen, W. Bao, L. Chang and G. Feng, *Chem. Eng. J.*, 2015, **263**, 9–19.
28 T. Zhang, F. Qiu, H. Chang, X. Li and J. Li, *Catal. Sci. Technol.*, 2016, **6**, 6294–6304.
29 J. Ma, Z. Si, D. Weng, X. Wu and Y. Ma, *Chem. Eng. J.*, 2015, **267**, 191–200.
30 G. A. Nasser, H. Adamu, A. I. Bakare, M. A. Sanhoob, H. Zhao, Z. H. Yamani, O. Muraza, E. Shafeai and J. W. Schwank, *Appl. Sci.*, 2023, **13**, 13001.
31 Q. Li, W. Cong, J. Zhang, C. Xu, F. Wang, D. Han, G. Wang and L. Bing, *Microporous Mesoporous Mater.*, 2022, **331**, 111649.
32 L. Bing, A. Tian, F. Wang, K. Yi, X. Sun and G. Wang, *Chemistry*, 2018, **24**, 7428–7433.
33 V. V. Bhat, C. I. Contescu, N. C. Gallego and F. S. Baker, *Carbon*, 2010, **48**, 1331–1340.
34 H. Jiang, B. Guan, H. Lin and Z. Huang, *Fuel*, 2019, **255**, 115587.
35 Y. Peng, J. Li, W. Si, J. Luo, Y. Wang, J. Fu, X. Li, J. Crittenden and J. Hao, *Appl. Catal., B*, 2015, **168–169**, 195–202.
36 D. Fang, F. He and J. Xie, *J. Energy Inst.*, 2019, **92**, 319–331.
37 X. Hu, J. Lin, X. Tan, C. Lin, Y. Zhang and W. Shan, *Chem. Eng. J.*, 2025, **520**, 165978.
38 X. Hu, J. Lin, X. Tan, C. Lin, H. Zhang, Y. Zhang and W. Shan, *Chem. Eng. J.*, 2025, **510**, 161874.
39 I. Heo, S. Sung, M. B. Park, T. S. Chang, Y. J. Kim, B. K. Cho, S. B. Hong, J. W. Choung and I.-S. Nam, *ACS Catal.*, 2019, **9**, 9800–9812.
40 Y. Wu, T. Andana, Y. Wang, Y. Chen, E. D. Walter, M. H. Engelhard, K. G. Rappé, Y. Wang, F. Gao, U. Menon, R. Daya, D. Trandal, H. An, Y. Zha and K. Kamasamudram, *Appl. Catal., B*, 2022, **318**, 121807.
41 S. Han, Q. Ye, S. Cheng, T. Kang and H. Dai, *Catal. Sci. Technol.*, 2017, **7**, 703–717.
42 I. Heo, Y. Lee, I.-S. Nam, J. W. Choung, J.-H. Lee and H.-J. Kim, *Microporous Mesoporous Mater.*, 2011, **141**, 8–15.
43 W. W. A. V. Salker, *Appl. Catal., A*, 2000, **203**, 8.
44 B. Wang, Y. Zhang, S. Chansai, A. Nadri, X. Ou, Q. Zhang, S. Xu, Y. Jiao and X. Fan, *Microporous Mesoporous Mater.*, 2025, **384**, 113429.
45 T. Zhang, H. Chang, Y. You, C. Shi and J. Li, *Environ. Sci. Technol.*, 2018, **52**, 4802–4808.
46 Y. Cui, Y. Wang, E. D. Walter, J. Szanyi, Y. Wang and F. Gao, *Catal. Today*, 2020, **339**, 233–240.
47 M. Tokushige and J. Ryu, *ACS Omega*, 2023, **8**, 32536–32543.
48 C. Wang, J. Wang, J. Wang, Z. Wang, Z. Chen, X. Li, M. Shen, W. Yan and X. Kang, *Catalysts*, 2018, **8**, 593.
49 C. Wang, C. Wang, J. Wang, J. Wang, M. Shen and W. Li, *J. Environ. Sci.*, 2018, **70**, 20–28.
50 J. Li, S. Ma, K. Ren and N. Xu, *Mol. Catal.*, 2023, **537**, 112920.
51 N. Zhu, Y. Shan, W. Shan, Y. Sun, K. Liu, Y. Zhang and H. He, *Environ. Sci. Technol.*, 2020, **54**, 15499–15506.
52 J. Li, S. Ma, N. Xu and T. Pei, *J. Phys. Chem. C*, 2022, **126**, 15191–15204.
53 Y. Liu, J. Qi, K. Zhu, H. Liu, X. Liu, M. Wang, M.-Y. Wang, J. Lv, S. Huang and X. Ma, *Catal. Sci. Technol.*, 2025, **15**, 2510–2518.
54 F. Goltl, A. M. Love, S. C. Schuenzel, P. Wolf, M. Mavrikakis and I. Hermans, *Phys. Chem. Chem. Phys.*, 2019, **21**, 19065–19075.
55 E. Borfecchia, K. A. Lomachenko, F. Giordanino, H. Falsig, P. Beato, A. V. Soldatov, S. Bordiga and C. Lamberti, *Chem. Sci.*, 2015, **6**, 548–563.
56 J. Devos, S. Robijns, C. Van Goethem, I. Khalil and M. Dusselier, *Chem. Mater.*, 2021, **33**, 2516–2531.
57 J. Luo, D. Wang, A. Kumar, J. Li, K. Kamasamudram, N. Currier and A. Yezerets, *Catal. Today*, 2016, **267**, 3–9.
58 Y. Jangjou, Q. Do, Y. Gu, L.-G. Lim, H. Sun, D. Wang, A. Kumar, J. Li, L. C. Grabow and W. S. Epling, *ACS Catal.*, 2018, **8**, 1325–1337.
59 J. Xue, X. Wang, G. Qi, J. Wang, M. Shen and W. Li, *J. Catal.*, 2013, **297**, 56–64.

60 Y. Ma, X. Wu, S. Cheng, L. Cao, L. Liu, Y. Xu, J. Liu, R. Ran, Z. Si and D. Weng, *Appl. Catal., A*, 2020, **602**, 117650.
61 W. Su, Z. Li, Y. Peng and J. Li, *Phys. Chem. Chem. Phys.*, 2015, **17**, 29142–29149.
62 P. N. R. Vennestrøm, T. V. W. Janssens, A. Kustov, M. Grill, A. Puig-Molina, L. F. Lundegaard, R. R. Tiruvalam, P. Concepción and A. Corma, *J. Catal.*, 2014, **309**, 477–490.
63 J. E. Schmidt, R. Oord, W. Guo, J. D. Poplawsky and B. M. Weckhuysen, *Nat. Commun.*, 2017, **8**, 1666.
64 A. Godiksen, F. N. Stappen, P. N. R. Vennestrøm, F. Giordanino, S. B. Rasmussen, L. F. Lundegaard and S. Mossin, *J. Phys. Chem. C*, 2014, **118**, 23126–23138.
65 J. Song, Y. Wang, E. D. Walter, N. M. Washton, D. Mei, L. Kovarik, M. H. Engelhard, S. Prodinger, Y. Wang, C. H. F. Peden and F. Gao, *ACS Catal.*, 2017, **7**, 8214–8227.
66 H. Gan, B. Wang, W. Ren, L. Chang, W. Bao, Z. Huang, L. Han and J. Wang, *J. Solid State Chem.*, 2024, **337**, 124782.
67 M. Xie, X. Xiao, J. Wang, J. Chen, H. Kang, N. Wang, W. Chu and L. Li, *Sep. Purif. Technol.*, 2023, **315**, 123617.
68 K. Xie, J. Woo, D. Bernin, A. Kumar, K. Kamasamudram and L. Olsson, *Appl. Catal., B*, 2019, **241**, 205–216.
69 N. Wilken, R. Nedyalkova, K. Kamasamudram, J. Li, N. W. Currier, R. Vedaiyan, A. Yezerets and L. Olsson, *Top. Catal.*, 2013, **56**, 317–322.
70 F. Giordanino, P. N. Vennestrom, L. F. Lundegaard, F. N. Stappen, S. Mossin, P. Beato, S. Bordiga and C. Lamberti, *Dalton Trans.*, 2013, **42**, 12741–12761.
71 Y. Yue, B. Liu, P. Qin, N. Lv, T. Wang, X. Bi, H. Zhu, P. Yuan, Z. Bai, Q. Cui and X. Bao, *Chem. Eng. J.*, 2020, **398**, 125515.
72 Z. Chen, L. Liu, H. Qu, B. Zhou, H. Xie and Q. Zhong, *J. Catal.*, 2020, **392**, 217–230.
73 S. Han, J. Cheng, C. Zheng, Q. Ye, S. Cheng, T. Kang and H. Dai, *Appl. Surf. Sci.*, 2017, **419**, 382–392.
74 V. V. Mesilov, S. L. Bergman, S. Dahlin, Y. Xiao, S. Xi, M. Zhirui, L. Xu, W. Chen, L. J. Pettersson and S. L. Bernasek, *Appl. Catal., B*, 2021, **284**, 119756.
75 F. Gao, D. Mei, Y. Wang, J. Szanyi and C. H. Peden, *J. Am. Chem. Soc.*, 2017, **139**, 4935–4942.
76 F. Gao, E. D. Walter, M. Kollar, Y. Wang, J. Szanyi and C. H. F. Peden, *J. Catal.*, 2014, **319**, 1–14.
77 B. Liu, D. Yao, F. Wu, L. Wei, X. Li and X. Wang, *Ind. Eng. Chem. Res.*, 2019, **58**, 20516–20527.
78 M. Wang, Z. Peng, C. Zhang, M. Liu, L. Han, Y. Hou, Z. Huang, J. Wang, W. Bao and L. Chang, *Catalysts*, 2019, **9**, 781.
79 I. K. P. Fejes, I. Hannus, A. Kiss and G. Schobel, *Catal. Lett.*, 1980, **14**, 7.
80 Y. J. Kim, J. K. Lee, K. M. Min, S. B. Hong, I.-S. Nam and B. K. Cho, *J. Catal.*, 2014, **311**, 447–457.

